Proceedings for the 2018 EUMETSAT Meteorological Satellite Conference,
17-21 September 2018, Tallinn, Estonia

A GEO-LEO (Geostationary and Low-Earth-Orbiting) Synergistic Approach to Aerosol Mapping: Towards a More Detailed and Higher Accuracy Aerosol Spatial and Temporal Distributions

Yi Qin[1*], Andy D. L. Steven[1], Martin Cope[2], Sam West[3], Jing Huang[2], Tim McVicar[4], Tim Malthus[1], Alex Held[5] and Michael A. Box[6]

[1] Coastal Development and Management, CSIRO Oceans and Atmosphere, Australia (contact: yi.qin@csiro.au)
[2] Climate Science Centre, CSIRO Oceans and Atmosphere, Australia
[3] Grids & Energy Efficiency Systems, CSIRO Energy, Australia
[4] Eco-hydrological Time-Series Remote Sensing, CSIRO Land and Water, Australia
[5] Centre for Earth Observation, CSIRO Astronomy and Space Science, Australia
[6] School of Physics, University of New South Wales, Australia

Abstract

Aerosols have a multitude of impacts on society, from daily life, to our environment and the climate. Aerosols remain one of the largest sources of uncertainty in climate modelling. Air pollution in the form of aerosols have major impacts on human health. Aerosols provide critical information for the correction of atmospheric effects on remote sensing imagery. Remote sensing provides a practical means to measure aerosols at global scales and at high spatial resolution. The new generation of geostationary satellites such as Himawari-8/9, HY-4, GOES-R and MTG-I, presents new opportunities to map aerosols in high temporal resolution with potentially high accuracy. However, aerosol mapping over land, especially over bright land such as the Australia continent, has been challenging due the dominating land surface which is highly variable over time, sun and view angles, and spectral wavelength. This work presents a multi-satellite approach combining GEO-LEO satellites to simultaneously retrieve aerosols and surface BRDF (Bidirectional Reflectance Distribution Function) over land.

GEO-LEO Virtual Dual View (VDV) Sensor Construction

A major challenge in aerosol retrieval is insufficient measurements from remote sensors, especially the most commonly available single-view sensors. One way to overcome this difficulty is by combining multiple satellites to effectively increase the simultaneous measurements. In this work, a procedure has been developed to construct virtual dual-view sensors to acquire dual-view observations, similar to a physical dual/multi-view sensor such as AATSR and MISR. This is

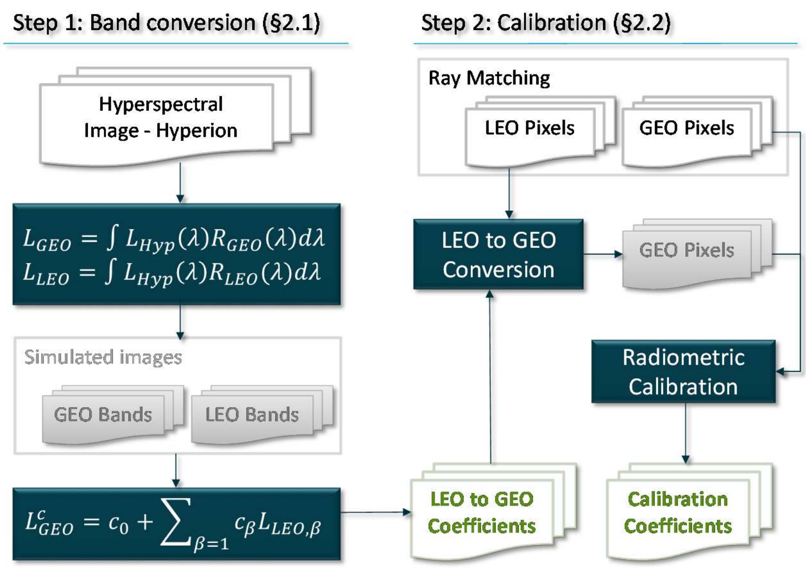

Figure 1 Flow chart showing the process implemented by Qin and McVicar (2018) to construct virtual-dual-view sensors from GEO-LEO sensors. White boxes represent the input images, and green texted boxes are the outputs of the process.

achieved by pairing AHI (Himawari-8/9) with low-earth-orbiting sensors such as MODIS. Due to the much higher (10 minutes) temporal resolution of the AHI, it is now possible to match the sensors within a very short time difference less than 5 minutes. However, the spectral bands of the involved sensors are very different, and the radiometric calibration may also be different. To reduce these differences, a procedure to unify the spectral bands of the sensors followed by a radiometric inter-calibration has been developed (Qin and McVicar 2018). Three virtual dual-view sensors, AHI-MODIS/Aqua, AHI-MODIS/Terra and AHI-VIIRS, have been constructed, with AHI-SGLI (GCOM-C) to be completed. The two-step procedure to construct VDV sensors is outlined in Figure 1 and discussed below.

In the first step, over 1270 representative Hyperion passes, uniformly spreading over the Australian continent, were used to simulate the spectral bands of the GEO and LEO sensors. These Hyperion images are aggregated from their original 30 meter resolution to 960 meters, approximating the resolution of MODIS and VIIRS, resulting in a total 1.3 million sample points. All valid sample pixels, including those over waters and a small amount of residual clouds, are used and together they represent a large range of spectral types. Using these simulated simultaneous GEO-LEO observations, relationships to estimate the radiance (L_{GEO}^{c}) of each of the five GEO bands (1 to 5) using one or more nearby LEO bands were established. Table 1 shows the LEO bands used, the conversion coefficients and the conversion error matrix. Among all the GEO-LEO band combinations, a maximum relative error of 2.74% at 95% of the sample points was found, and the majority (9) of the 15 cases have maximum relative error less than 1% at 95% sample, and only 2 are above 2%. The mean bias is negligible for all cases. The representativeness of the Hyperion sample, the low regression error and negligible bias indicate that the conversion is reliable and accurate over the whole continent.

In the second step, ray-matching was used to collect near-simultaneous observations from each of the GEO-LEO sensor pairs. Around the GEO's sub-satellite point, and for each LEO orbit, there is a moment when the observed point and the LEO and GEO satellites are linearly aligned providing a pair

AHI Bands (μm)	LEO Sensor & Bands	Conversion Coefficients				Mean Error		Mean Bias		95% Error	
		c_0	c_1	c_2	c_3	Abs. ×10⁴	Rel. %	Abs. ×10⁴	Rel. %	Abs. ×10⁴	Rel. %
MODIS/Aqua											
0.47	b03 b04	-0.5969	0.9748	0.0316		3.9	0.25	-0.7	-0.02	10.2	0.65
0.51	b11 b10	-0.9021	0.4864	0.5170		8.0	0.53	-0.5	0.04	22.4	1.61
0.64	b01 b04	-0.0342	0.9544	0.0541		3.0	0.17	0.0	0.00	9.5	0.44
0.86	b02	-0.0022	1.0041			1.4	0.07	0.0	-0.02	3.8	0.19
1.60	b06 b07	-0.0506	0.9423	0.1630		12.8	0.79	1.1	-0.17	32.7	2.57
MODIS/Terra											
0.47	b03 b04	-0.6256	0.9736	0.0344		4.2	0.26	-0.4	-0.00	10.8	0.68
0.51	b11 b10	-0.9015	0.4963	0.5065		8.0	0.53	-0.5	0.04	22.5	1.62
0.64	b01 b04	-0.0335	0.9525	0.0564		3.2	0.18	0.0	0.00	10.2	0.47
0.86	b02	-0.0066	1.0040			1.6	0.05	0.0	-0.00	5.0	0.13
1.60	b06 b07	-0.0526	0.9408	0.1717		13.8	0.85	1.2	-0.17	35.4	2.74
VIIRS											
0.47	M03 M02 M04	-0.0749	0.6942	0.3538	-0.0323	2.8	0.18	-0.3	-0.01	7.2	0.54
0.51	M03 M02 M04	-0.0191	0.9974	-0.2677	0.2300	5.1	0.36	0.5	0.04	13.2	1.07
0.64	I01 M05	0.0026	0.9821	0.0176		0.3	0.02	0.0	0.00	1.0	0.05
0.86	M07 M08	-0.0388	1.0189	-0.0308		11.9	0.51	2.5	0.01	36.2	1.57
1.60	M10 M11 M08	-0.0077	0.9873	-0.0367	0.0108	6.1	0.28	-0.4	0.01	16.4	0.83

Table 1 Results for the LEO bands to AHI bands conversions. Shown are the MODIS band(s) and VIIRS band(s) used to convert to each AHI band, the coefficients, the mean fitting errors and biases, and the maximum error for 95% of the sample points. Unit for c_0 is W/m^2sr. Absolute errors and biases are in top-of-atmosphere reflectance.

Band (CWL,μm)	N	Slope(b_b) value	Slope(b_b) Std-err	Intercept(a_b) value	Intercept(a_b) Std-err	p	Regression r^2	Regression Fit-err	Regression Fit-bias
AHI–MODIS/Aqua									
0.47	2071	0.9701	0.0010	1.6810	0.2187	0.0000	0.9928	5.6907	0.0753
0.51	387	0.9376	0.0052	0.8404	0.3030	0.0055	0.9792	1.1248	0.1063
0.64	2079	1.0220	0.0011	1.0833	0.1597	0.0000	0.9928	5.0954	0.1592
0.86	1831	1.0328	0.0014	0.2842	0.1000	0.0045	0.9895	2.9091	0.1979
1.60	1750	1.0437	0.0020	0.2245	0.0213	0.0000	0.9852	0.4844	0.0288
AHI–MODIS/Terra									
0.47	2074	0.9421	0.0009	3.7255	0.1873	0.0000	0.9938	4.9675	-0.2338
0.51	667	0.9700	0.0036	-0.3080	0.2321	0.1846	0.9831	1.4156	0.0172
0.64	2081	1.0238	0.0009	1.0666	0.1260	0.0000	0.9941	4.1796	-0.1202
0.86	2033	1.0051	0.0010	0.7126	0.0811	0.0000	0.9933	2.6798	-0.0669
1.60	1855	1.0205	0.0017	0.3626	0.0185	0.0000	0.9882	0.4226	-0.0049
AHI–VIIRS									
0.47	757	1.0145	0.0009	2.0390	0.2340	0.0000	0.9974	4.2912	-0.0160
0.51	766	0.9718	0.0009	0.5203	0.2353	0.0270	0.9974	4.2117	-0.1146
0.64	1201	1.0305	0.0008	0.4704	0.1381	0.0007	0.9972	3.6981	-0.0235
0.86	1299	1.0142	0.0008	0.3519	0.0811	0.0000	0.9968	2.3058	-0.1036
1.60	2143	1.0390	0.0016	0.0299	0.0167	0.0732	0.9894	0.4148	0.0099

Table 2 Radiometric inter-calibration results. Shown are the AHI band (centre wavelength), number of valid matching points, slope, intercept and their standard error of, intercept p-value, the regression r-square, fitting error and bias. Units for intercept, its standard error, and the fitting error and bias are *W/m²sr*. Source: (Qin and McVicar 2018).

of surface measurements of the same point in the same view angle with essentially the same sun angle, within ±5 minutes. This very close match between GEO-LEO observations allows the use of both clear and cloudy pixels, providing a wide radiance range necessary for robust calibration. Finally, the matching LEO bands were converted to the corresponding GEO bands, and an inter-calibration between the paired sensors was conducted. Table 2 shows the inter-calibration results, derived using data from July 2015 to February 2017 (20 months). It shows that the procedure is reliable and accurate as indicated by the high correlation, low error and negligible bias in the regression; these calibration coefficients are also comparable with previous studies (Tabata et al. 2016; Yu and Wu 2016).

Aerosol and BRDF Retrieval

The dual view data from these VDV sensors doubles the amount of measurements, which significantly reduces the difficulties in aerosol retrievals caused by insufficient measurements. Nevertheless, to model the surface directional reflectance a minimum of three parameters is probably required for

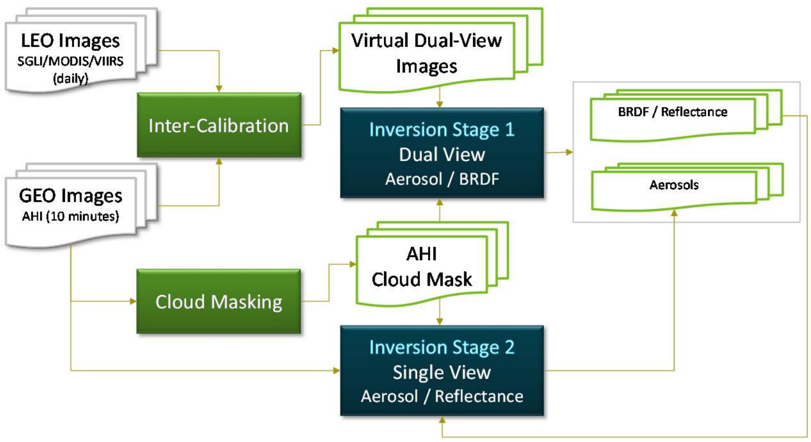

Figure 2 the work flow of the aerosol and BRDF retrieval algorithm, using virtual-dual-view dataset derived from the procedure described in Figure 1.

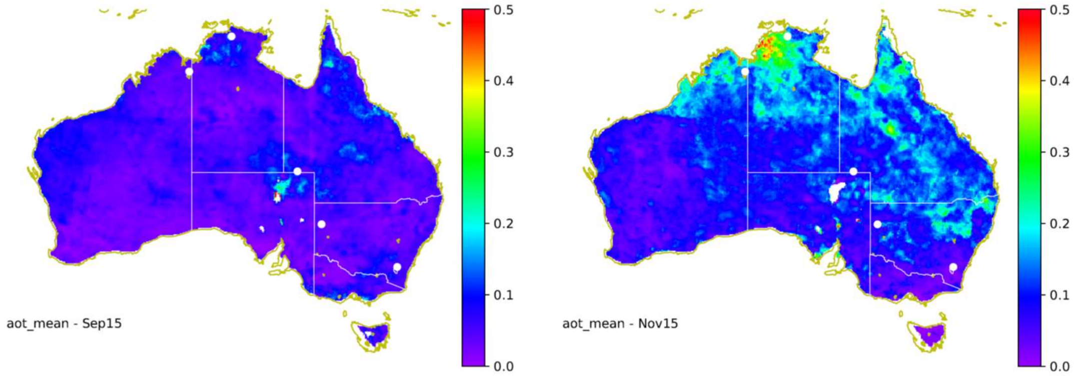

Figure 3 Monthly mean aerosol optical depth for September and November 2015.

each band, and therefore the total number of variables from the surface and the atmosphere is still much higher than the number of measurements. In a previous study by Qin et al. (2015) it was found that, while the magnitude of the surface reflectance may change rapidly, the shape of the BRDF remains stable for substantially long period of time, from months to years. This provides us the possibility to further reduce the number of variables to be inverted, by assuming the stability of the BRDF shape.

Using the virtual dual view dataset, a new inversion algorithm is being developed to simultaneously retrieve AOD (Aerosol Optical Depth), aerosol type and BRDF. Figure 2 shows the overall work flow of the algorithm. Centre to the algorithm is a two-stage inversion where in the first stage dual-view observations are used to simultaneously retrieve aerosol and surface BRDF. This is largely based on a previous development (Qin et al. 2015) for AATSR (ENVISAT). From this first stage, the long term BRDF shape function is retrieved, in addition to up to three updates of aerosol and surface reflectance daily for each location, from the three pairs of GEO-LEO VDV sensors. Using the BRDF shape function and daily updates of reflectance from stage-1, in the second stage all GEO passes could be inverted to produce high frequency aerosol maps over the continent. This stage is currently being developed.

Examples of continental wide aerosol distributions, from stage-1, are shown in Figure 3. It shows the highly seasonal nature of Australian aerosol events. During winter and portion of spring and autumn, there are few aerosol activities and the whole continent shows only low level of background aerosols as seen in Figure 3 (left), with

Site	AHI-MODIS (Terra)		AHI-MODIS (Aqua)		AHI-VIIRS		All Sensors	
	N	Err	N	Err	N	Err	N	Err
Jabiru	150	0.043	86	0.043	86	0.033	322	0.041
Lake Argyle	188	0.045	125	0.031	102	0.024	415	0.036
Birdsville	229	0.044	123	0.021	177	0.025	529	0.032
Fowlers Gap	302	0.037	230	0.028	232	0.027	764	0.032
Canberra	121	0.029	80	0.027	92	0.023	293	0.026
All Sites	990	0.040	644	0.029	689	0.026	2323	0.033

Table 3 Aerosol optical depth retrieval validation against AERONET. Shown are the number of matchup points (N), the mean AOD error against AERONET, for the individual AHI-GEO VDV's, and for all sensor mean. The period of validation is from July 2015 to July 2017.

the exception of Lake Eyre region (centre of continent) which is a major source region of dust, and over the top end where the fire season has started. However, by the time of November, Figure 3 (right) shows much elevated level of aerosols over the top end, where the annual biomass burning has reached its peak. Relatively high level of aerosols are also observed over the Northwest to Southeast path, which is known a major aerosol transportation path.

While the algorithm is still being developed, preliminary validation has been conducted against the AERONET data. Table 3 summarizes the mean retrieval error, for individual VDV sensors, and for all sensors averaged. Among the 8 AERONET sites available, 5 of them are found to have significant number of matchups and therefore are shown in the table, and three others are ignored due to very few matchups (12 at Lucinda, 26 at Lake Lefroy and none at Learmonth). Matchups are collected for the inversion cell closest to each site, and for AERONET records within half hour of satellite observation. Retrieval vs. AERONET scatter plots and time series plots are shown in Figure 4. Overall, the mean error of 0.033 as shown in Table 3 is comparable to that of the AATSR algorithm which has a mean error of 0.03. However, the new algorithm has shown to be more robust with the successful inversion rate improved to now nearly 100%, ensuring that aerosol data is obtained for all cloud-free pixels. On this basis, further development is being conducted to retrieve aerosols at every 10 minutes.

Summary

This work presents a GEO-LEO synergistic approach to simultaneously retrieve aerosol and BRDF over land. To support the algorithm, a procedure has been developed to create GEO-LEO virtual dual-view (VDV) remote sensors. By firstly unifying the paired GEO-LEO spectral bands followed by a radiometric inter-calibration of the unified bands using the ray-matching method, it has been demonstrated that the virtual dual view sensors are capable of providing dual-view observations similar to that of a physical dual/multi-view sensor such as AATSR and MISR. This is indicated by the

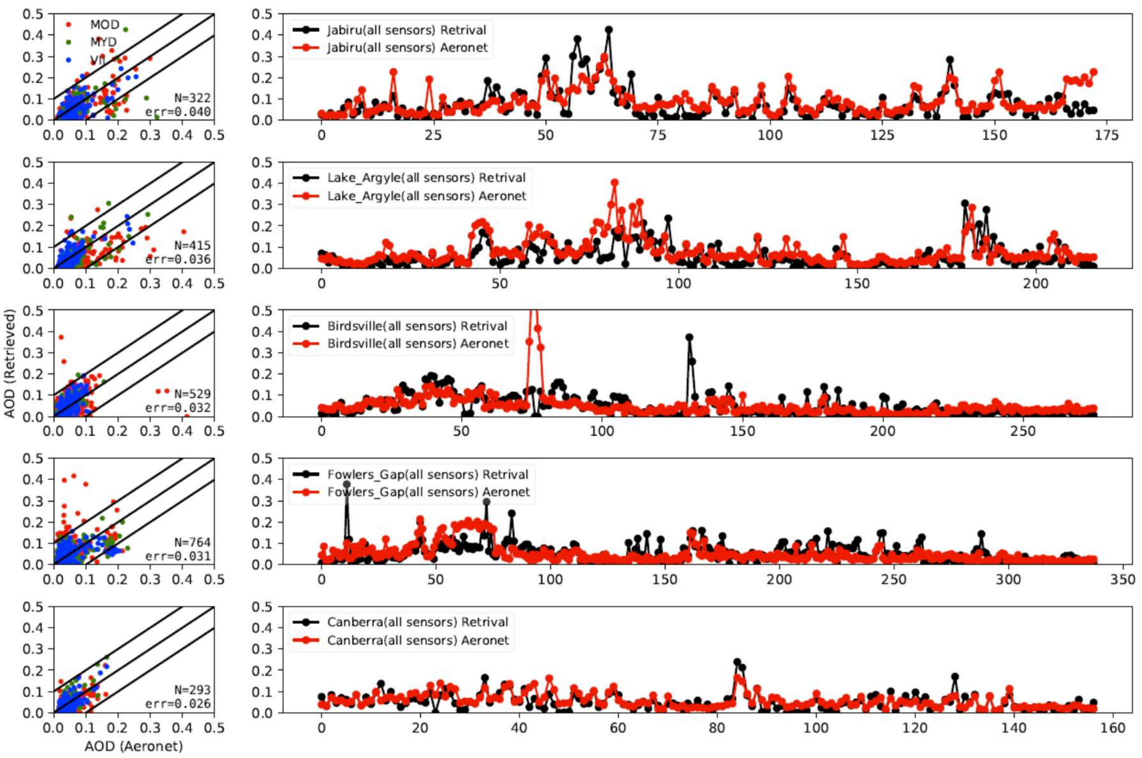

Figure 4 Left: AOD (retrieved) vs. AOD (AERONET), for retrievals from individual VDV sensors; Right: Daily mean time series where all retrievals in a day are averaged.

high accuracy in band unification, and high correlation and low bias in radiometric inter-calibration. However, by constructing a constellation of VDV sensors, the revisit can be increased to multiple times every day, an advantage compared to the (multi-)daily revisits of the physical dual-/multi-view sensors.

A new two-stage aerosol/BRDF retrieval algorithm is being developed, where in the first stage dual view data are used to simultaneously retrieve aerosol and surface BRDF, while in the second stage, supplemented by the BRDF information from stage-1, only the AHI data is used allowing retrieval of aerosols in every 10 minutes. So far stage-1 has been implemented and stage-2 is being developed. Preliminary results obtained from stage-1 is promising. The aerosol optical depth validation against AERONET has shown a mean retrieval accuracy of 0.033, comparable to that of the AASTR algorithm, based on which the current stage-1 algorithm is developed.

In addition to support the retrieval of aerosols, the GEO-LEO VDV approach also allows the tracking of relative temporal radiometric drift between the paired sensors. Figure 5 shows the relative changes of calibration slope and constant over a 20 month period. In this case it shows all the sensors (i.e., AHI (Himawari 8/9), MODIS (Aqua and Terra) and VIIRS) are very stable, in agreement with previous studies (Doelling et al. 2015; Wang and Cao 2016; Wu et al. 2016). The change of slope is less than 1% for most cases, well within the 2% MODIS calibration uncertainty (Xiong et al. 2018). Large

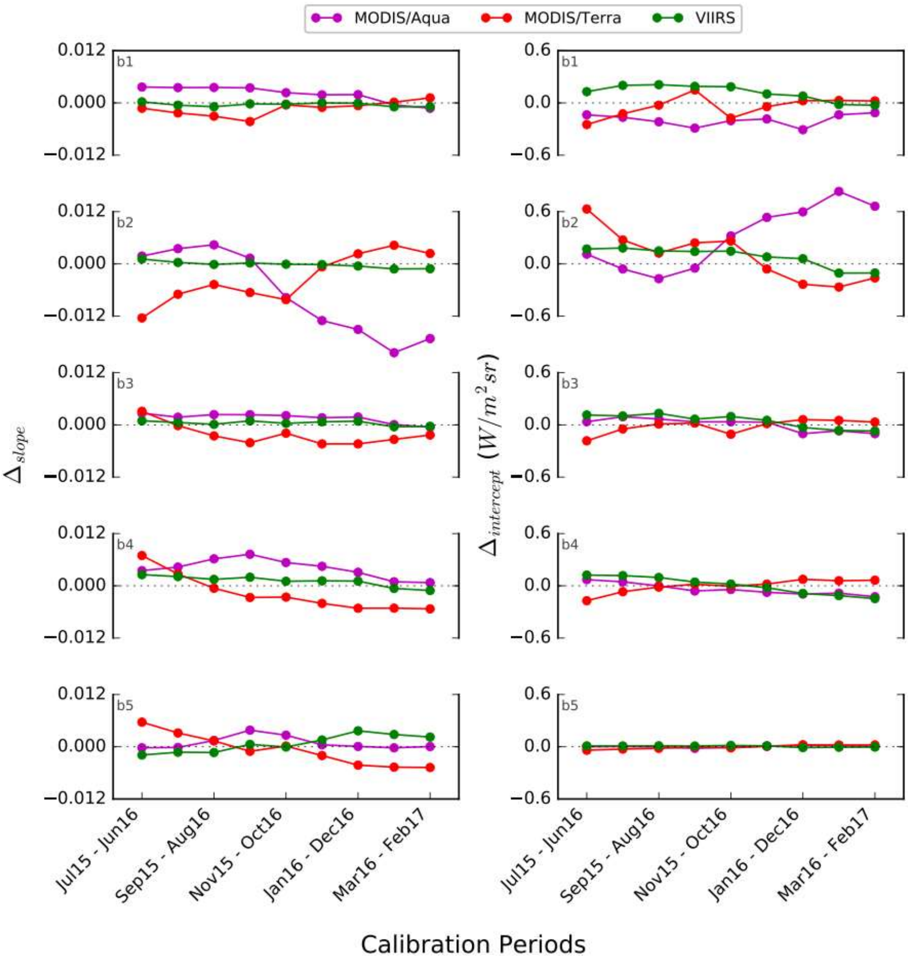

Figure 5 Temporal trend of the inter-calibration slope (left) and intercept (right) for the three sensor-pairs and AHI bands 1 to 5 (0.47, 0.51, 0.64, 0.86 and 1.61μm, from top to bottom respectively) calculated for moving-window 12-month periods incrementing by one month. Shown in the plots are the slope / intercept of each period subtracted by the slope / intercept of the whole-period-calibration (**Error! Reference source not found.**), for each band and sensor pair, respectively.

variation for the 0.51 μm AHI-MODIS bands is likely regression fluctuation, as indicated by the corresponding variations between slope and constant, due to the use of the ocean colour bands (10 and 11) which have small radiance range resulting in about ¾ GEO-LEO matched observations being removed due to sensor saturation.

The VDV procedure described in this work is also readily applicable to calibrate multiple GEO sensors against one (or set of) reference LEO sensor, leading to globally consistent and continuous observations by the GEO sensors. Further, by then combining multiple radiometrically-consistent GEO sensors, other LEO sensors can potentially be calibrated against the same (set of) reference LEO sensor(s), leading to consistent multi-GEO-multi-LEO databases of original bands (single-view) or unified bands (dual-view).

Acknowledgement

This work is funded by the Costal Development and Management Program of CSIRO Oceans and Atmosphere as part of a collaboration project between CSIRO and GCOM-C mission, JAXA. The Department of environment, land, water and planning, Victoria, Australia provided partial funding through a Dynamic Smoke Modelling and Community Impacts of Smoke project. The authors acknowledge the effort of Dr Ross Mitchell to establish and maintain the AERONET sites used in the validation of AOD. Dr David Jupp organized the Hyperion data set which is gratefully thanked. AHI images were provided by the Japanese Meteorology Agency through Australian Bureau of Meteorology. MODIS images were acquired using the LAADS web service (https://ladsweb.nascom.nasa.gov) of NASA Distributed Active Archive Centre (DAAC). VIIRS images were acquired using NOAA Comprehensive Large Array-Data Stewardship System (CLASS) web service. Australian National Computational Infrastructure (NCI) and CSIRO Scientific Computing provided computational resources and assistance.

References

Doelling, D.R., Wu, A.S., Xiong, X.X., Scarino, B.R., Bhatt, R., Haney, C.O., Morstad, D., & Gopalan, A. (2015). The Radiometric Stability and Scaling of Collection 6 Terra-and Aqua-MODIS VIS, NIR, and SWIR Spectral Bands. *IEEE Transactions on Geoscience and Remote Sensing, 53* (8), 4520-4535 (doi:4510.1109/Tgrs.2015.2400928)

Qin, Y., & McVicar, T.R. (2018). Spectral band unification and inter-calibration of Himawari AHI with MODIS and VIIRS: Constructing virtual dual-view remote sensors from geostationary and low-Earth-orbiting sensors. *Remote Sensing of Environment, 209*, 540-550 (doi:510.1016/j.rse.2018.1002.1063)

Qin, Y., Mitchell, R., & Forgan, B.W. (2015). Characterizing the Aerosol and Surface Reflectance Over Australia Using AATSR. *IEEE Transactions on Geoscience and Remote Sensing, 53* (11), 6163-6182

Tabata, T., Andou, A., Bessho, K., Date, K., Dojo, R., Hosaka, K., Mori, N., Murata, H., Nakayama, R., Okuyama, A., & Takahashi, M. (2016). Himawari-8/AHI latest performance of navigation and calibration. In, *Proc. SPIE 9881, Earth Observing Missions and Sensors: Development, Implementation, and Characterization IV, 98812J (May 2, 2016); doi:10.1117/12.2240200*

Wang, W.H., & Cao, C.Y. (2016). Monitoring the NOAA Operational VIIRS RSB and DNB Calibration Stability Using Monthly and Semi-Monthly Deep Convective Clouds Time Series. *Remote Sensing, 8* (1), 32 (doi:10.3390/rs8010032)

Wu, A.S., Xiong, X.X., Cao, C.Y., & Chiang, K.F. (2016). Assessment of SNPP VIIRS VIS/NIR Radiometric Calibration Stability Using Aqua MODIS and Invariant Surface Targets. *IEEE*

Transactions on Geoscience and Remote Sensing, 54 (5), 2918-2924 (doi:2910.1109/Tgrs.2015.2508379)

Xiong, X., Angal, A., Barnes, W.L., Chen, H., Chiang, V., Geng, X., Li, Y., Twedt, K., Wang, Z., Wilson, T., & Wu, A. (2018). Updates of Moderate Resolution Imaging Spectroradiometer on-orbit calibration uncertainty assessments. In (pp. 18, doi:org/10.1117/1111.JRS.1112.034001): SPIE

Yu, F.F., & Wu, X.Q. (2016). Radiometric Inter-Calibration between Himawari-8 AHI and S-NPP VIIRS for the Solar Reflective Bands. *Remote Sensing, 8* (3), 165 (doi:110.3390/rs8030165)